

THE FIRST HIGH RESOLUTION X-RAY SPECTRUM OF CYG X-1: SOFT X-RAY IONIZATION AND ABSORPTION

N. S. SCHULZ¹, W. CUI², C. R. CANIZARES¹, H. L. MARSHALL¹, J. C. LEE¹, J. M. MILLER¹ AND W.H.G. LEWIN¹

Submitted for publication in The Astrophysical Main Journal

ABSTRACT

We observed the black hole candidate Cyg X-1 for 15 ks with the High-Energy Transmission Grating Spectrometer aboard the *Chandra X-ray Observatory*. The source was observed during a period of intense flaring activity, so it was about a factor of 2.5 brighter than usual, with a 0.5–10 keV (1–24 Å) luminosity of 1.6×10^{37} erg s^{−1} (at a distance of 2.5 kpc). The spectrum of the source shows prominent absorption edges, some of which have complicated substructure. We use the most recent results from laboratory measurements and calculations to model the observed substructure of the edges. From the model, we derive a total absorption column of $6.21 \pm 0.22 \times 10^{21}$ cm^{−2}. Furthermore, the results indicate that there are ~ 10 –25% abundance variations relative to solar values for neon, oxygen and iron. The X-ray continuum is described well by a two-component model that is often adopted for black hole candidates: a soft multicolor disk component (with $kT = 203$ eV) and a hard power law component (with a photon index of ~ 2). Comparing the fit results to those of the hard and soft states, we conclude that the source was in a transitional state. Finally, the spectrum also shows the presence of faint emission lines which could be attributed to highly ionized species.

Subject headings: stars: individual (Cyg X-1) — stars: black holes — X-rays: stars — X-rays: photo-electric absorption binaries: close — accretion: accretion disks — accretion: winds — techniques: spectroscopic

1. INTRODUCTION

Cygnus X-1 was the first X-ray source to be identified with a binary system and where radial velocity measurements indicated a mass of the compact companion large enough to be a black hole rather than a neutron star (Webster and Murdin 1972, Bolton 1972). The period of the binary was determined optically to be about 5.6 days. The system consists of an O9.7 Iab supergiant with a mass in excess of $\sim 20 M_{\odot}$ in orbit with a black hole of a mass in excess of $\sim 7 M_{\odot}$ (see Tanaka and Lewin (1995) for a detailed review). Cyg X-1 is therefore intrinsically different from the majority of known black hole candidates (BHCs) whose stellar components, where known, are much less massive. Nevertheless, Cyg X-1 is generally regarded as an archetypical BHC; its spectral and temporal properties are often used to identify other BHCs, although so far the only direct evidence for the black hole nature comes from the dynamical determination of its mass via radial velocity measurements. The X-ray emission from Cyg X-1 is likely due to the release of gravitational energy of matter that is accreted by the black hole from the companion star. The mass accretion process is thought to be mediated by a so-called "focussed wind" from the companion star that is close to but not quite filling its Roche lobe (Gies and Bolton 1986). Tentative evidence for wind accretion is provided by the observed orbital modulation of X-ray and radio emission from Cyg X-1 (Kitamoto et al. 2000; Wen et al. 1999; Brocksopp et al. 1999a; Priedhorsky et al. 1995; and Holt et al. 1979).

In the soft (< 10 keV) X-ray band, the X-ray spectrum of Cyg X-1 can be described roughly by a two-component model: a multicolor disk component and a power law component. The former accounts for the X-ray emission from the hot inner portion of an optically thick, geometrically thin accretion disk,

while the latter is thought to be due to inverse Comptonization of soft photons (e.g., from the accretion disk) by energetic electrons in an optically thin configuration. The exact shape of the continuum defines two distinct spectral states for Cyg X-1: the hard and the soft state. The source is usually found in the hard state, where the spectrum is dominated by the power law component with a photon index of ~ 1.7 (see review by Tanaka & Lewin 1995, and references therein). The detection of the weaker disk component is difficult during this state. The most reliable results came from the observations of the source with ASCA (Ebisawa et al. 1996), which gave a temperature of the disk of only about $kT = 100$ eV.

Occasionally, for yet unknown reasons, Cyg X-1 experiences a transition to the soft state, where the disk component grows stronger and the power law component steepens to a typical photon index of about 2.5 (Tanaka & Lewin 1995). The most recent spectral state transition occurred in 1996 (Cui et al. 1996). The source was observed simultaneously by ASCA and RXTE near the end of the hard-to-soft transition. The results indicated that the disk component was indeed dominant below 10 keV and the temperature of the disk was around $kT = 400$ eV (Cui et al. 1998).

The detection of an iron K α line and/or absorption edge has been reported for Cyg X-1. For instance, a broad emission line seen at ~ 6.2 keV was interpreted to be a red-shifted and broadened K α line of cold iron (Barr, White and Page 1985; Tanaka 1991; Done et al. 1992). A narrow emission line was also detected at 6.4 keV in the hard state, which is thought to originate in the fluorescent emission from the cold part of the accretion disk (Kitamoto et al. 1990; Tanaka 1991; Ebisawa et al. 1992; Ebisawa et al. 1996). A similar emission line was also seen near the soft state (during the 1996 state transition) but at

¹Center for Space Research, Massachusetts Institute of Technology, Cambridge, MA 02139.

²Department of Physics, Purdue University, West Lafayette, IN 47907.

~ 6.6 keV, which was interpreted as emission from highly ionized iron (Cui et al. 1998). Iron K α line emission has become one of the most useful tools for probing the strong gravitational field near a black hole. The detection of a gravitationally distorted line would provide strong evidence for the existence of a black hole. Such a line has been reported for the Seyfert 1 galaxy MG-6-30-15 (Tanaka et al. 1995), but has never been detected in Cyg X-1.

In this paper we present the first high resolution X-ray spectra of Cyg X-1 obtained with the High Energy Transmission Gratings Spectrometer (HETGS, Canizares et al. 2001, in preparation) onboard the *Chandra* X-ray Observatory (*Chandra* hereafter) during its early phase of the mission. In this paper we take a fresh look at the soft part of the spectrum below 10 keV, particularly below 1 keV. We report the detection of prominent absorption edges in the spectrum of Cyg X-1, as well as weak emission lines due to highly ionized species.

2. CHANDRA OBSERVATIONS AND DATA REDUCTION

Cyg X-1 was observed with the HETGS on 1999 October 15 (start time 05:47:21 UT) continuously for 15 ks. For a general description of the HETGS we refer to available *Chandra* X-ray Center (CXC) documents³. In this section we outline the overall properties of this observation, which was performed using the Advanced CCD Imaging Spectrometer (ACIS, Garmire et al. 2001, in preparation) in standard timed event mode, but with alternating frame times to accommodate the high source flux.

The HETG disperses about half of the incident photons into 1st and higher order spectra, which are recorded with an array of 6 CCDs at the focal plane of the telescope. All other photons generate an image in the zeroth order, which is located at the focus of the telescope. Every set of seven CCD frames of 3.3 sec was followed by a short frame of 0.5 sec. This resulted in an effective exposure of 11.5 ks in long frame mode and 0.3 ks in short frame mode. Separate event lists were delivered by the CXC standard processing. Throughout this paper, we distinguish between a long frame observation and a short frame observation, although the reader should always keep in mind that both observations were performed during the same time period. In order to avoid frame dropouts due to telemetry saturation, we blocked the zeroth order events electronically from being transmitted. Therefore standard source detection is not possible and we ignored any products from standard processing higher than level 1.

The determination of the zeroth order position is crucial for the calibration of the wavelength scales because this position defines its zero point. We calculated this position by fitting the dispersed images of the Medium Energy Gratings (MEG) and High Energy Gratings (HEG) and then determined the intersections of the fit with the zero order readout trace of the CCD. The intersections for the MEG and HEG were determined to be within 0.2 detector pixels. From this, we deduce an accuracy of the zero order position of 0.002 \AA in MEG and 0.001 \AA in HEG 1st order. This uncertainty is negligible when compared to the overall wavelength calibration, which has been verified on orbit to be better than $\sim 0.05\%$ (Canizares et al. 2001, in preparation). The worst case uncertainty in the wavelengths then is 0.011 \AA in the MEG 1st order near the O K edge, 0.008 \AA in the HEG 1st order near the Ne K edge and 0.003 \AA in the MEG 3rd order near the Mg K edge. We processed the event lists into

grating (level 1.5) event lists using available CXC software. From there on we used the Chandra Interactive Analysis of Observations package (CIAO 2.1⁴) and custom software to produce our final grating spectra. We computed aspect corrected exposure maps for each spectrum which allow us to calculate the effective area of the spectrometer to obtain absolute fluxes. Current systematic uncertainties of the effective area calibration are ~ 10 to 20% ; in some cases we were able to correct for local flux enhancements by comparing opposite sides of the dispersion.

High X-ray fluxes cause photon pileup in X-ray CCD devices. In the case of Cyg X-1 the flux is so high that photons pile up even in the grating spectra during long-frame exposures. Pileup occurs when two or more photons of the same energy are registered almost simultaneously and thus identified by the CCD device as one photon of the summed energies of the registered photons. In the case of the grating spectra this means that photons from 1st order spectra are registered in higher CCD channels which are coincidentally identified for photons from higher order spectra. The 1st order spectra below $\sim 14 \text{ \AA}$ (MEG) and $\sim 10 \text{ \AA}$ (HEG) are depleted of photons, which then populate the second and third order spectra at wavelengths below half and one third of the wavelengths, respectively. The MEG 3rd order spectrum below $\sim 4.6 \text{ \AA}$ is therefore 'contaminated' by photons piled up from MEG 1st order.

3. LIGHT CURVE

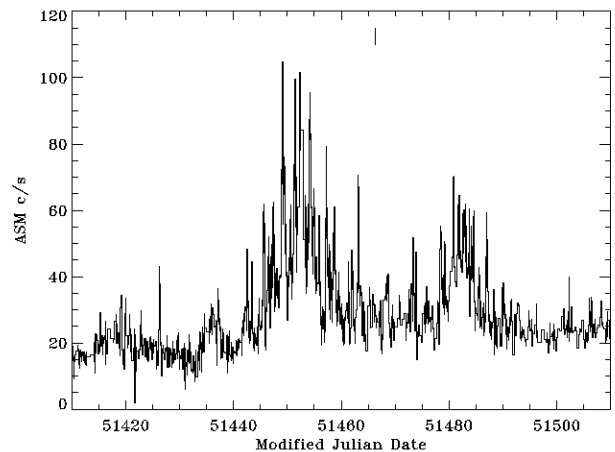


FIG. 1.— ASM light curve of Cyg X-1 of the soft flares in the vicinity of the HETGS observation. The vertical line at the top indicates the time of the *Chandra* observation.

Cyg X-1 was observed during a period when it produced frequent X-ray flares. Flaring activity is common for the source, as shown by the long-term monitoring of the source by the All-Sky Monitor (ASM) aboard *RXTE* (see Fig. 1). However, X-ray flares are usually brief, and are therefore difficult to catch in short observations. Consequently, they are poorly understood due to the lack of data. The *Chandra* observation now provides us with a rare opportunity to examine the properties of Cyg X-1 during such an event. Figure 1 shows a portion of the ASM light curve for a time span of about 100 days during which the short (15 ks) *Chandra* observation was performed. The time of the *Chandra* observation is indicated in the figure. As can be seen, Cyg X-1 was engaged in heavy flaring activity and the observation lies in between two giant flares. We also note that there are

³<http://asc.harvard.edu/udocs/docs/docs.html>

⁴<http://cxc.harvard.edu>

gaps in the ASM coverage. Some brief mini-flares could therefore have been missed during the ASM coverage. The *Chandra* light curve is difficult to analyse because the source appeared at a rate of over 200 cts per sec in the HETGS 1st orders and light curves are systematically affected when we include these data. Excluding all grating data affected by pileup (with a confidence level of better than 99.9%), we obtained a light curve for the bandpass above 6 Å, which showed variability of roughly 20% over the observation.

4. SPECTRAL ANALYSIS

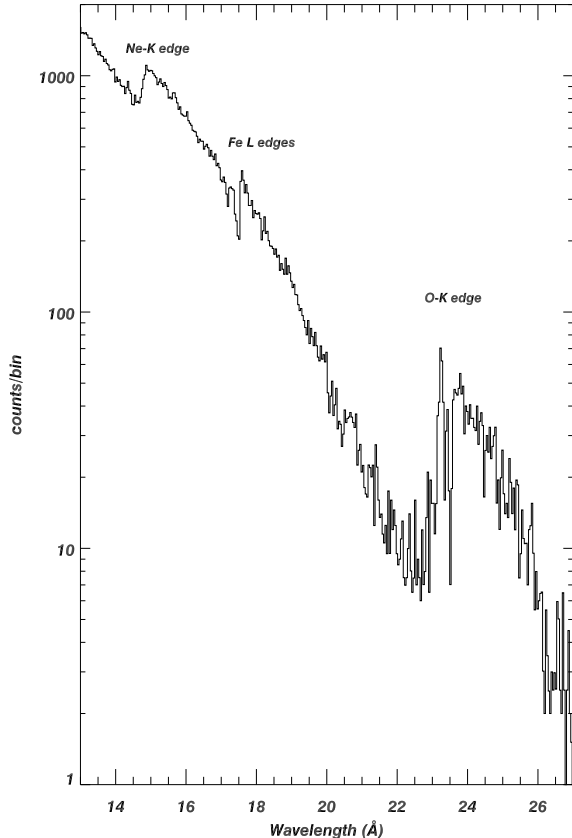


FIG. 2.— The MEG spectrum in the 13 - 27 Å band, where it is unaffected by pileup. The binsize is 0.04 Å. The data are not corrected for instrumental effects.

Major portions of the 1st order grating spectra were severely piled up and only of limited quality and not all wavelengths can be used to study the broad band continuum shape in the long frame observation. In the following analysis, we look in detail at the observed neutral edges from which we are able to derive reliable column densities of the absorbing material. We use these column densities to fit the spectral continuum in the subsequent section. Using the optical depth of each detected edge from the spectrum, we derive the column density for that particular element. Using the combined results for various elements, we then determine an overall column density, as well as abundance variations of the elements in the absorbing gas. Finally we identify residual absorption and emission features.

4.1. Photoelectric Absorption

In low resolution detectors the detailed shape of photoelectric absorption edges were never resolved and therefore were largely ignored. In a high-resolution spectrum of the

Crab Nebula using the Focal Plane Crystal Spectrometer on-board *Einstein* Schattenburg and Canizares (1986) presented the first detailed X-ray spectrum near the O K edge and found marginal evidence for a resonant $1s-2p$ absorption line from atomic oxygen. Paerels et al. (2001) showed with *Chandra* Low Energy Transmission Grating data near the neutral oxygen edge of another X-ray binary, 4U 0614+091, there is considerable structure due to absorption lines from atomic oxygen as well as other molecular compounds. For the case of Cyg X-1, we observe similar complex substructures which we quantify by comparing them with expected structure obtained from laboratory measurements as well as from calculations.

The MEG count spectrum (Fig. 2) shows the photo-electric absorption edges of O K, Fe L, and Ne K of Cyg X-1. A detailed study of the structure of photoelectric absorption in observations of a sample including other bright X-ray binaries will be presented by Schulz et al. (2001, in prep).

Neutral absorption column densities are directly proportional to the optical depth of the neutral edge. The latter is defined by

$$\tau = \ln(f_{\text{high}}/f_{\text{low}}), \quad (1)$$

where f_{high} is the X-ray flux on top of the edge at the high wavelength side and f_{low} is the X-ray flux at the bottom of the edge at the low wavelength side. We emphasize that this optical depth corresponds to the total amount of photo-electric absorption, which includes the interstellar medium in the line of sight as well as a possible intrinsic contribution by the source itself. We observe edges at O, Fe, Ne, and Mg. The data allow to directly measure the optical depths in the cases of O, Fe, and Ne. The Mg edge is visible but the bins for f_{high} and f_{low} have large uncertainties. The Si edge does not appear significantly in the data. Table 1 shows the expected and measured values of the edges and the measured optical depths from these edges. We quadratically added a systematic uncertainty of one spectral resolution bin to the wavelength uncertainty, which also dominates the uncertainty of the edge value.

The edges exhibit considerable substructure, which we describe in detail below. We first determined the optical depths τ of the O-K, Fe-L, and Ne-K edges using equation 1. The optical depth ratios between these edges showed some deviations to the ones expected for abundances derived using the polynomial fit parameters from Morrison & McCommon (1983) as implemented in XSPEC using the cross sections from Verner et al. (1993). We also applied a continuum model fit derived from the short frame data using a pre-determined value for N_H derived mainly from a first assessment of the Ne-K optical depth, which shows the least structure. Assuming a solar abundance relative to hydrogen as stated by Morrison and McCommon (1983) we find a best value of $N_H = 6.21 \pm 0.22 \times 10^{21} \text{ cm}^{-2}$. For elements other than Ne, O, and Fe we use the solar abundances relative to hydrogen. In the case of Ne, O, and Fe we use the long frame data to tweak the optical depths by adjusting abundances. The abundance adjustment factor a_z is shown in Table 1. For O and Fe we find a lower abundance of $\sim 7\%$ and $\sim 25\%$, respectively. For Ne we find a higher abundance of 11%. From the final adjusted models we then determined the optical depths τ_m shown in table 1. We have also calculated the column density for each ion species Z , defined as

$$N_z = \frac{\tau_m}{\sigma_z}, \quad (2)$$

where σ_z are the atomic photoelectric cross sections. We use

TABLE 1
POSITIONS AND OPTICAL DEPTHS FROM PHOTO-ELECTRIC EDGES

edge	λ_o Å	λ_m Å	τ_m	NH_z cm^{-2}	a_z^2
O K	23.34 ¹	23.15 \pm 0.02	2.226 \pm 0.133	3.92 \pm 0.23 $\times 10^{18}$	0.93
Fe L 3	17.51 ²	17.56 \pm 0.02	1.098 \pm 0.086	1.55 \pm 0.12 $\times 10^{17}$	0.75
Fe L 2	17.19 ²	17.23 \pm 0.02	0.307 \pm 0.027	1.46 \pm 0.12 $\times 10^{17}$	-
Fe L 1	14.66 ¹	14.66 \pm 0.02	0.079 \pm 0.017	-	-
pure Fe L	17.44 ³	17.41 \pm 0.02	0.058 \pm 0.012	8.24 \pm 1.72 $\times 10^{15}$	-
Fe _x O _y	17.64 ⁴	17.66 \pm 0.02	0.025 \pm 0.009	4.49 \pm 1.61 $\times 10^{15}$	-
Ne K	14.30 ¹	14.32 \pm 0.02	0.343 \pm 0.011	9.43 \pm 0.32 $\times 10^{17}$	1.11
Mg K	9.50 ¹	9.49 \pm 0.02	0.088 \pm 0.032	3.67 \pm 1.34 $\times 10^{17}$	1.00
Si K	6.74 ¹	6.74 \pm 0.01	0.036 \pm 0.028	2.31 \pm 1.81 $\times 10^{17}$	1.00

¹from Bearden & Burr 1967, ²from Kortright & Kim 2000, ³from Brown 2000, ⁴from Crocombet et al. 1995 ⁵ abundance adjustment factor

mostly the cross sections from Verner et al. 1993, except for Fe, where we have new cross sections from Kortright & Kim (2000). The final spectral model was generated by computing the absorption edges using τ_m and also by adding single gaussians for local absorption dips.

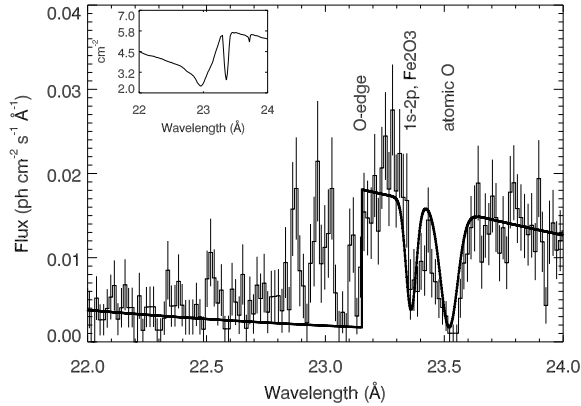


FIG. 3.— A MEG view of the O K edge region. The curve represents the model. The inset shows the effective area of the MEG around the O K edge.

4.1.1. The O K edge

Structure in the O K edge is difficult to assess with the MEG because the effective area of the instrument is relatively low and affected by instrumental O features. The source is easily detected longward of the edge (see Fig. 2); statistical uncertainties in the data are of the order of $< 30\%$ (Figure 3). Shortward of the edge, the spectrum is very faint. The most probable position of the O K edge appears at 23.15 Å, which is lower than the expected value of 23.31 Å (Bearden and Burr 1967), but consistent with a most recent observation of Cyg X-1 (Marshall et al. 2001). The value of the O-edge in this observation is difficult to assess, because we observe excess emission around 23 Å. We consider two likely interpretations. First, the excess emission would result from a systematic error in the effective area model (see inset in Fig. 3), which is dominated by the O K edges of polyimide in the ACIS filter and the MEG support material. Based on pre-launch calibration, however, systematic errors in the HETGS effective area should be no more than 50%, while an error four times or more would be required to

eliminate the feature at 23 Å. Second, we cannot rule out the possibility that some of the excess emission consists of emission lines from Cyg X-1 (see section 4.3). Given the results by Marshall et al. 2001, the latter interpretation is more likely. The feature at 23.36 Å coincides with a resonance feature in polyimide, but there is a significant residual, which may be identified with the 1s-2p transition from oxygen in Fe₂O₃ (Wu et al. 1997). Most prominently the large absorption dip with a FWHM of 0.08 Å at 23.51 Å due to the 1s-2p transition in atomic oxygen. This feature was marginally detected by Schattenburg and Canizares (1983) in a Crab Nebula observation, but appeared prominently in the LETG observation of X 0614+091 (Paerels et al. 2001).

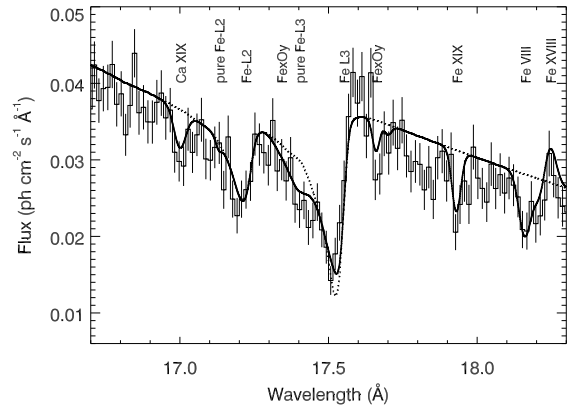


FIG. 4.— A portion of the MEG spectrum showing the photo electric Fe L III and II edges. The solid curve is the final model, the dotted line shows the shape of the Fe 3 and 2 edges from Kortright and Kim (2000).

4.1.2. The Fe L edges

Iron is the most abundant element that has its L absorption in the HETGS bandpass. The Fe-L1 edge is due to transitions from the 2s level, Fe-L2 from the 2p_{1/2}, and Fe-L3 from the 2p_{3/2} level. The Fe-L3 edge is usually strongest, the Fe-L1 edge is weakest. Figure 4 shows the Fe-L edge region in the MEG spectrum. We clearly observe that these edges have narrow absorption features, which cannot be described by a single step function. The Fe-L1 edge region is shown in Figure 5. The shapes of the Fe-L edges were measured by various groups

using metallic iron of various purity as well as iron oxides (Kortright & Kim 2000, Brown 2000, Schwickert et al. 1998, Crocombette et al. 1995). These studies indicate that the position of the Fe L edges depend on whether the sample is oxidized or metallic. We measured the position of the Fe L3 edge (defined to be the top of the edge) to be 17.56 \AA . This position is consistent with recent measurements of metallic Fe film by Kortright & Kim (2000), but is between results from Fe foils of very high purity (Brown 2000) and Fe oxides (Crocombette et al. 1995). We used new experimental cross sections from Kortright & Kim (2000) in the absorption model shown in Figure 4. This model represents the overall observed shape of the edges quite well, with some caveats. First of all, the column density of Fe is $\sim 25\%$ lower than expected from the Morrison & McCompton representation. We observe some slight deviations from the shape predicted by Kortright & Kim (2000), which may indicate that Fe exists in various forms, or that the edge has superimposed intrinsic emission and absorption lines. We observe additional, but very weak features around 17.41 \AA and 17.66 \AA , which match the positions that Brown (2000) determined from an extremely pure Fe sample as well as those from Fe oxides (Crocombette et al. 1995), respectively. We added absorption from these forms of Fe into the model assuming the same shape of the cross section as from the Kortright data. With this approach we would recover about 7% of the missing Fe. Wilms, Allen and McCray (2000) list an amount comparable to the remaining 18% as the difference between the solar abundance of Fe and the one in the interstellar medium. There are also faint features from ionized species (see section 4.3), which appear in emission as well as absorption. From our analysis in section 4.3 it seems likely that these distortions are due to emission and absorption from highly ionized iron, so we simply added Gaussian line components to the model. The normalizations were determined by fitting single Gaussians to the data, while the widths were fixed to the MEG spectral resolution.

4.1.3. The Ne K-, Mg K-, and Si K edges

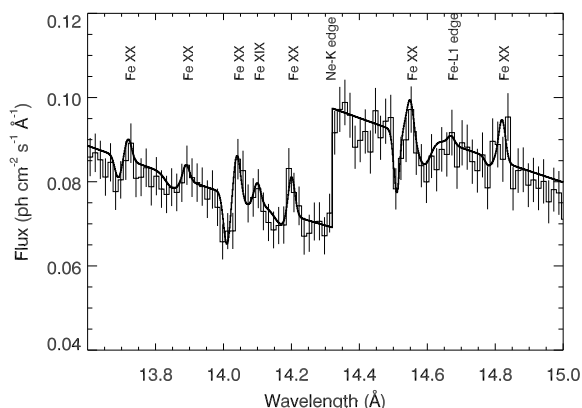


FIG. 5.— A portion of the MEG spectrum which shows the photoelectric edge of Ne K and numerous weak ionized iron lines.

The Ne K edge (see Figure 5) can be very well modeled using the Verner et al. (1993) cross section, since it appears only in gaseous form. The wavelength has been measured in the laboratory to $14.302 \pm 0.003 \text{ \AA}$ in agreement with the calculated value of 14.30 \AA (Bearden and Burr 1967). We measure a value of $14.32 \pm 0.02 \text{ \AA}$, which is consistent with the

expected value above. It is also consistent with the value observed in X0614+091 (Paerels et al. 2001), which however has a very large uncertainty. There is considerable substructure in the vicinity, which we identify as emission lines (see section 4.3) similar to the features in the vicinity of the O and Fe edges.

The Mg K and Si K edges (see Figure 6) appear at wavelengths where the MEG and HEG spectra are significantly piled up and we have to rely on the spectrum from the MEG 3rd order, which has an order of magnitude lower efficiency. Both edges are modeled using the Verner et al. (1993) cross sections and the abundance factor a_z in Table 1 is set to 1.

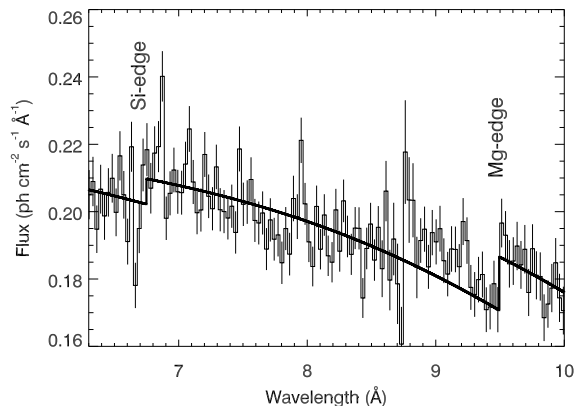


FIG. 6.— A portion of the MEG 3rd order spectrum which shows the photoelectric edges of Mg K and Si K.

4.2. The X-ray Continuum

For the determination of the continuum spectral shape we use the short as well as the full frame observations. The short frame data provide us with a pileup free continuum at the expense of exposure. We therefore determined the continuum in two steps. First we fit the spectra from the short frame observation using the XSPEC package in order to determine the overall spectral shape and also define the spectral model to fit the continuum. Second, we test the fit on a spectrum obtained by combining pileup-free portions of the long frame observations, where we combine portions from the MEG 1st ($14\text{--}26 \text{ \AA}$), HEG 1st ($10\text{--}14 \text{ \AA}$), and MEG 3rd ($6\text{--}10 \text{ \AA}$) order. Both, short frame and long frame spectra, have their limitations: the short frame spectra have large statistical uncertainties, the long frame data are statistically very significant but only accurate for wavelengths $> 6 \text{ \AA}$.

A simple power law does not give a good fit even to the short frame data. A second power law component improved the fit to the short-frame data considerably, but leaves significant residuals when applied to the long-frame data. Using the multicolor disk model (as used by Cui et al. 1997) as a second component we obtain an excellent fit to the data ($\chi^2 < 1$; 2206 d.o.f). The result, shown in Figure 7, also includes the photoelectric absorption models. The power law has an index of 1.95 ± 0.07 , the disk component has a temperature of $kT = 203 \pm 4 \text{ eV}$. The total absorbed flux is $1.03 \times 10^{-8} \text{ erg cm}^{-2} \text{ s}^{-1}$ between 0.5 and 10 keV ($\sim 1 - 25 \text{ \AA}$), with the disk component contributing about 11%. Assuming a distance of 2.5 kpc to the source, we determine a luminosity of the disk blackbody component of $5.34 \times 10^{36} \text{ erg s}^{-1}$ and a total luminosity of $1.61 \times 10^{37} \text{ erg s}^{-1}$. Compared with the properties of the source in the hard and soft states (e.g., Ebisawa et al. 1996, Cui et al. 1998), our results

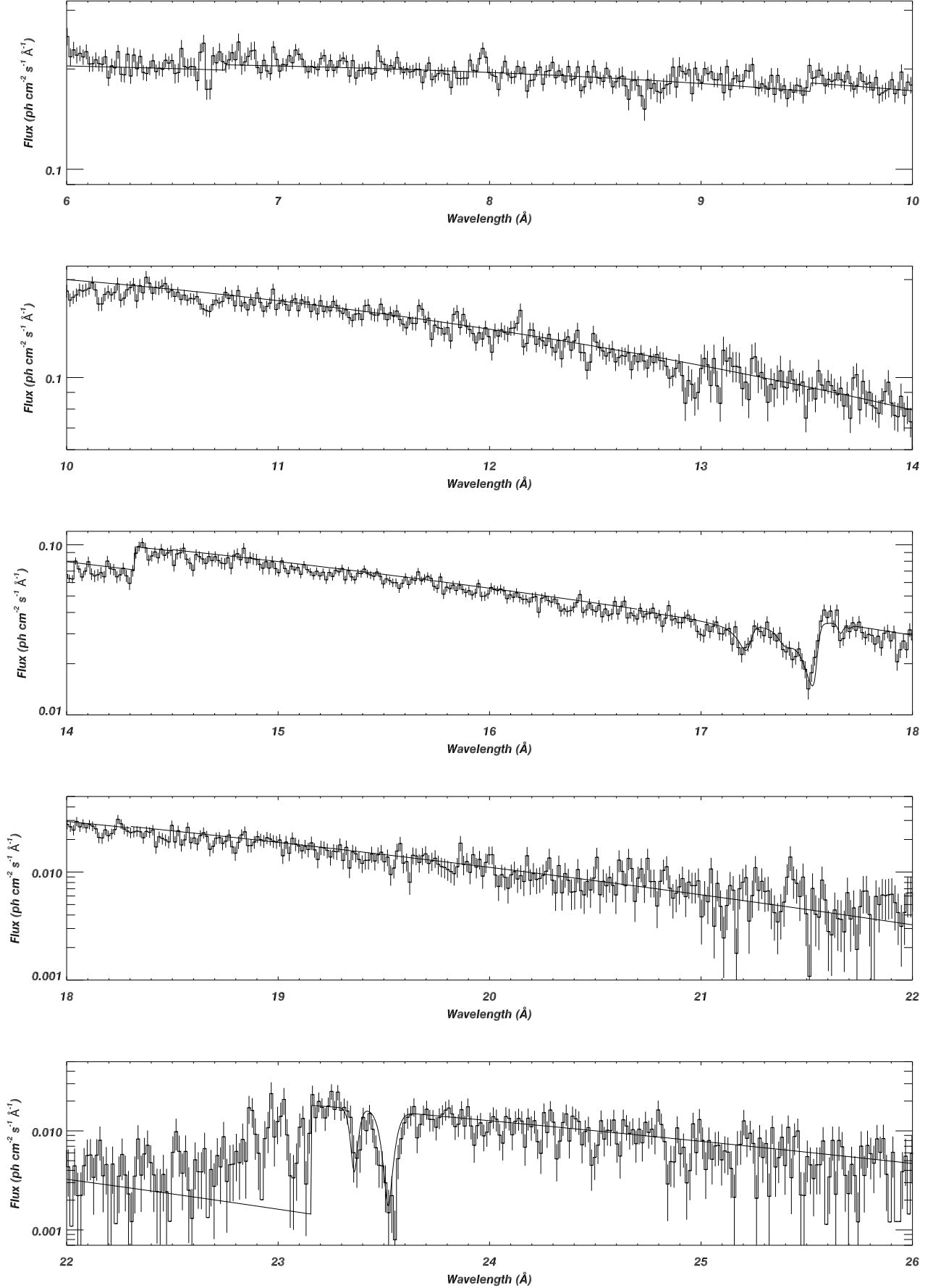


FIG. 7.— The broadband HETGS spectrum between 6 and 26 \AA . The continuum model was fitted with a disk blackbody plus power law model. The lower three panels are from the MEG 1st order spectrum, the second one from top shows a portion of the HEG 1st order spectrum, the top panel shows the MEG 3rd order spectrum.

clearly show that the source was in a transitional state, as expected from the ASM light curve (see Fig. 1).

4.3. Narrow Emission and Absorption Features

TABLE 2
WEAK AND NARROW LINE FEATURES FOR WAVELENGTHS > 6
 \AA

λ_{em}^1 \AA	Ion	$\log T^2$ (k)	S/N	λ_{abs}^1 \AA	ion	S/N
				6.65	Si XIII	4.1
6.88	Si X	6.3	3.4			
7.09	Mg XII	7.0	3.3			
7.31	Mg XI	6.8	2.3			
	Ni XXV	7.2				
7.47	Mg XI	6.8	2.1			
	Fe XXIII	7.2				
7.68	Fe XXIII	7.2	-			
7.98	Fe XXIV	7.3	3.2			
				8.05	Fe XXII	2.1
				8.19	Fe XXII	3.0
				8.42	Mg XII	2.3
				8.72	Fe XXIII	2.8
8.76	Fe XXIII	7.2	2.8			
9.22	Mg XI	6.8	4.3			
				10.15	Fe XX	3.1
				10.65	Fe XXIII	5.3
11.67	Fe XVIII	6.8	2.3			
11.84	Fe XXII	7.1	2.3			
11.88	Fe XVIII	6.9	3.3			
				12.01	Fe XXI	2.4
12.14	Ne X	6.8	2.2			
				12.48	Fe XXI	4.2
12.50	Fe XXII	7.1	2.9			
				12.94	Fe XX	4.5
				12.99	Fe XX	4.4
13.04	Fe XXII	7.1	2.5			
13.14	Fe XX	7.0	2.2			
				13.50	Fe XX	2.0
13.56	Ne IX	6.6	2.1			
	Fe XX	7.0				
				13.69	Fe XX	2.3
14.04	Fe XX	7.0	3.0			
14.20	Fe XX	7.0	3.3			
				14.49	Fe XIX	4.7
14.55	Fe XX	7.0	4.1			
14.83	Fe XX	7.0	2.1			
16.42	Fe XX	7.0	3.0			
				17.00	Ca XIX	3.6
				17.41	Fe XVIII	3.0
17.54	Fe XIX	6.9	3.8			
				17.93	Fe XIX	4.3
				18.18	Fe XVIII	4.4
18.25	Fe XVIII	6.8	2.7			
				18.81	?	2.8
18.83	O VIII ³	6.5	2.0			
21.43	O VII ³	6.3	3.4			
22.52	O V	6.2	2.7			
22.86	O IV	5.7	4.1			
23.05	S XIV	6.5	3.3			
23.10	S XIII	6.4	3.5			

¹from SPEX 1999 line list

²temperature of maximum emissivity

³possibly blue shifted by 2350 km s⁻¹

There are a variety of emission and absorption features in the vicinity of the edges (Figures 3-5). A few are also visible in figure 7. Nearly all of these features are weak, detected with a signal to noise (S/N) ratio of less than 5. The S/N ratio in Table 2 is defined as

$$S/N = \frac{\sum f_i^l}{\sqrt{\sum (\sigma_i^c)^2}}, \quad (3)$$

where f_i^l is the flux of a line in the spectral bin i and σ_i^c the significance of the continuum in that bin and the sum is over the line width. The flux in each bin is the value of the bin subtracted by the value of the model in that bin multiplied by the width of the bin. The uncertainty in each bin of the underlying continuum was determined from the square root of the model value folded through exposure and effective area. We exclude all bandpass regions where pileup effects are significant. The detected emission as well as absorption features and the positions (λ_{em} for emission, λ_{abs} for absorption), tentative identifications, and detection significances are listed in table 2. The identifications were made using the line list from Mewe (1994). Features with a S/N ratio near 2 are not very significant, but in the context of the ones with higher ratios have valid identifications. We identify ion species mostly from intermediate to highly ionized Fe with ionization stages between Fe XVIII and Fe XXIV. In column 3, we also list the temperature corresponding to the peak emissivity of the transition. These indicate temperature values between 1.5 and 20 Million K. Many of the features are seen in the Figures 3 to 5, but we also show the 11.5 - 13.6 \AA bandpass from the HEG spectrum in Figure 8. All the features are narrow and do not appear resolved by the MEG resolution. The observed flux range is 2.1 - 15×10^{-5} ph cm⁻² s⁻¹.

There are several difficulties associated with the identifications of these weak lines. In Figures 3-8 we see that there are also absorption features and many of them seem to be associated with an adjacent emission line which gives the impression of a P Cygni type line profile, such as has been observed in Cir X-1 (Brandt and Schulz 2000). We list those in the right part of table 2. Note, that Marshall et al (2001) also report strong absorption lines in another HETGS observation of Cyg X-1. In general, identifications in the wavelength band below 16 \AA are not entirely unique, because the line density is so high, increasing the likelihood of misidentification. At longer wavelengths (> 16 \AA), the Fe transition forest thins so identifications are more straightforward.

Figure 9 shows a weak detection at 21.43 \AA . This line coincides with a line from Ca XVI at 21.44 \AA , which given the temperature distribution in column 3 of table 2, is an unlikely identification in the absence of other nearby Ca lines. We tentatively attribute this feature to the O VII He-like resonance line, which would mean a shift corresponding to about -2350 km s⁻¹. Similarly we detect a fainter feature at 18.83 \AA , with some absorption at 18.81 \AA , which are both not identified. It could be identified with the O VIII Lyman α transition, if it is also blue-shifted by 2350 km s⁻¹.

5. SUMMARY AND DISCUSSION

The first high resolution X-ray spectrum of Cyg X-1 obtained with *Chandra* shows various features, which will be discussed in more detail below. In the following we briefly summarize the main results from the *Chandra* observations. From resolved neutral edges of various elements we derive a very accurate column density for Cyg X-1 of $6.21 \pm 0.22 \times 10^{21}$ cm⁻². The results indicate that there are abundance variations for Ne, O and Fe of the order of 10 to 20% relative to solar values; the deficiencies in Fe and O are roughly consistent an abundance distribution of

results indicate that the source was in a state that is similar to the transitional period between the hard and soft states. This is consistent with the fact that the source was observed during a period of strong flaring.

The detection of modulations caused by the orbital period in the light curves and hardness ratios of Cyg X-1 (e.g., Wen et al. 1999) can be interpreted as being caused by a varying absorption optical depth through the companion wind with the binary motion. Gies and Bolton (1986) estimated that the terminal velocity of the wind is $\sim 1500 \text{ km s}^{-1}$ based on the radiatively driven wind model of Castor, Abbott, and Klein (1975). Recent *Chandra* observations of stellar winds from massive O-stars (Schulz et al. 2000, Kahn et al. 2001, Waldron and Cassinelli 2001) find strong X-ray line emission with luminosities quite similar of the faint line features we observe in the Cyg X-1 spectrum and we find it very likely that some of these are signatures from the companion wind. The P Cygni type appearance of some of the lines bolster the case for a wind. P Cygni X-ray lines have been observed in the spectra of Cir X-1 (Brandt and Schulz 2000) as well as, - tentatively - in Cyg X-3 (Liedahl et al. 2000). In Cir X-1 the profiles are thought to originate in a high velocity disk wind, while in Cyg X-3 the extremely strong wind of the Wolf-Rayet companion star may

generate such lines. Previously, Pravdo et al. (1980) observed wavelength shifts in IUE observations of HD226868, the companion of Cyg X-1. Extreme blue shifts of Si IV and C IV lines up to -1570 km s^{-1} and -2270 km s^{-1} were attributed to the stellar wind of the companion. However, recent *Chandra* observations of massive O stars have detected much smaller blueshifts (Schulz et al. 2000, Waldron and Cassinelli 2001, Kahn et al. 2001, Cassinelli et al. 2001). It is therefore difficult to associate the derived -2300 km s^{-1} shift of the O VII line with the stellar wind. For Cyg X-1 it seems more likely that we observe line emission from various different emission regions, which produce a complex pattern of emission and absorption in the X-ray spectrum. Future high resolution observations covering different orbital phases and with longer exposures may be used to identify the features that vary with the orbital motion and thus shed light on their physical origin.

The authors want to thank the MIT HETG team and the *Chandra* X-ray Center for its support. This research is funded by contracts SV-61010 and NAS8-39073. WHGL also gratefully acknowledges support from NASA. W.C. has also been supported by NASA through the LTSA grant NAG5-9998.

REFERENCES

- Balućńska M., and Hasinger G., 1990, *A&A*, 241, 439
 Barr P., and van der Woerd H., 1990, *ApJ*, 352, L41
 Barr P., White N.E., and Page C.G., 1985, *MNRAS*, 216, 65
 Bearden J.A., and Burr A.F., 1967, *Rev. Mod. Phys.*, 39, 125
 Bolton C.Y., 1972, *Nature*, 235, 271
 Brandt W.N., and Schulz N.S., 2000, *ApJ*, 544, 123
 Brocksopp C., Fender R.P., Larinov V., Lyuty V.M., Tarasov A.E., Pooley G.G., Paciesas W.S., and Roche P., 1999a, *MNRAS*, 309, 1063
 Brocksopp C., Tarasov, A. E., Lyuty, V. M., & Roche, P. 1999b, *A&A*, 343, 861
 Brown 2000, <http://www-mp.phy.cam.ac.uk/people/vlad/thesis.html>
 Cassinelli J., Miller N.A., Waldron W.L., MacFarlane J.J., and Cohen D.H., 2001, *ApJ*, submitted
 Castor J., Abbott D.C., and Klein R.I., 1975, *ApJ*, 195, 157
 Crocombette, Pollak M., Jollet F., Thromat N., and Gautier-Soyer M., 1995, *Phys. Rev. B*, 52, 3143
 Cui W., Ebizawa K., Dotani T., and Kubota A., 1998, *ApJ*, 493, L75
 Cui W., Heindl W.A., Rothschild R.E., Zhang S.N., Jahoda K., and Focke W., *ApJ*, 474, L57
 Done, C., Mulchaey, J. S., Mushotzky, R. F., & Arnaud, K. A. 1992, *ApJ*, 395, 275
 Done C., and Zycki P.T., 1999, *MNRAS*, 305, 457
 Ebisawa K., Ueda Y., Inoue H., Tanaka Y., and White N.E., 1996, *ApJ*, 467, 419
 Ebisawa K., Inoue H., Mitsuda K., Nagase F., Tanaka Y., Yaqoob T., and Yoshida K., 1992, in *Frontiers of X-ray Astronomy*, ed. Y. Tanaka. and K. Koyama (Tokyo), 301
 Gies D.R., and Bolton C.Y., 1986, *ApJ*, 304, 389
 Holt, S. S., Kaluzienski, L. J., Boldt, E. A., & Serlemitsos, P. J. 1979, *ApJ*, 233, 344
 Kahn S.M., Leutenegger M., Cottam J., Rauw G., Vreux J.M., den Boggende T., Mewe R., and Guedel M., 2001, *A&A*, 365, L312
 Kitamoto, S., Egoshi, W., Miyamoto, S., Tsunemi, H., Ling, J. C., Wheaton, Wm. A., & Paul, B., 2000, *ApJ*, 531, 546
 Kitamoto S., Takahashi K., Yamashita K., Tanaka Y., and Nagase F., 1990, *PASJ*, 42, 85
 Kitamoto S., Miyamoto S., Kondo Y., Taware Y., and Nakagawa M., 1984, *PASJ*, 36, 731
 Kortricht J.B., and Kim S.-K., 2000, *Phys. Rev. B*, 62, p. 12216
 Liedahl D.A., Sako M., Paerels F., Mc Collogh M.L., Elsner R.F., Schulz N.S., and Cohen D.H., 2000, *HEAD*, 32.2503
 Marshall F.E., Mushotzky R.F., Petre R.F., and Serlemitsos P.J., 1993, *ApJ*, 419, 301
 Marshall H.L., Schulz N.S., Cui W., and Canizares C.R., 2001, *ApJ Letters*, in prep.
 Mewe R., 1994, *SPEX version 1.0/Rev. 4.0*
 McLaughlin B.M., and Kirby K.P., 1998, *J. Phys. B: At. Mol. Opt. Phys.*, 31, 4991
 Morrison R., and McCommon D., 1983, *ApJ*, 278, 1082
 Paerels F., Brinkman A.C., van der Meer R.L.J., et al., 2001, *ApJ*, 546, 338
 Pravdo S.H., White N.E., Becker R.H., Kondo Y., Boldt E.A., Holt S.S., Serlemitsos P.J., and McCluskey G.E., 1980, *ApJ*, 237, 71
 Priedhorsky, W. C., Brandt, S., Lund, N. 1995, *A&A*, 300, 415
 Remillard R.A., and Canizares C.R., 1984, *ApJ*, 278, 761
 Schulz N.S., Canizares C.R., et al., 2001, *ApJ*, in prep.
 Schulz N.S., Canizares C.R., Huenemoerder D., and Lee J.C., 2000, *ApJ*, 545, 135
 Schulz N.S., 1999, *ApJ*, 511, 304
 Schwickert M.M., Guo G.Y., Tomaz W.L., O'Brian W.L., and Harp G.R., 1998 *Phys. Rev. B*, 58, 4289
 Sunyaev R.A., and Trümper J., 1979, *Nature*, 279, 506
 Tanaka Y., 1991, in *Lecture Notes in Physics* 385, p. 98, ed. A. Treves (Springer)
 Tanaka Y., et al. 1995, *Nature*, 375, 659
 Tanaka Y., and Lewin W.H.G., 1995, in *X-ray Binaries*, ed. W.H.G. Lewin, J. van Paradijs, and E.P.J. van den Heuvel (Cambridge: Cambridge Univ. Press), 252
 Verner D.A., Yakovlev D.G., Band I.M., and Trzhaskovskaya M.B., 1993, *Data Nucl. Data Tables*, 55, 233
 Waldron W., and Cassinelli J., 2001, *ApJ*, in press
 Webster B.L., and Murrin P., 1972, *Nature*, 235, 37
 Wen L., Cui W., and Bradt H.V., 2001, *ApJ*, 546, L105
 Wen L., Cui W., Levine A., and Bradt H.V., 1999, *ApJ*, 525, 968
 Wilms J., Allen A., and McCray R., 2000, *ApJ*, 542, 914
 Wu, Z.-Y., Gota S., Jollet F., Pollak M., Gautier-Soyer M., and Natoli C.R., 1997, *Phys. Rev. B*, 55, 2570